

# Evidence of air-induced surface transformation of atomic step-engineered sapphire in relation to epitaxial growth of 2D semiconductors

Received: 18 December 2024

Accepted: 20 August 2025

Published online: 26 September 2025

 Check for updates

Wei Fu<sup>1,2</sup> , Jianwei Chai<sup>1</sup>, Hiroyo Kawai<sup>3</sup> , Thathsara Maddumapatabandi<sup>1,2</sup>, Fabio Bussolotti<sup>1,2</sup>, Ding Huang<sup>1,2</sup>, Rainer Lee<sup>1,2</sup>, Siew Lang Teo<sup>1</sup> , Hui Ru Tan<sup>1</sup> , Calvin Pei Yu Wong<sup>1</sup> , Anqi Sng<sup>1</sup>, Yunjie Chen<sup>1</sup>, Chit Siong Lau<sup>1,2,4</sup> , Mingsheng Zhang<sup>1</sup> , Henry Medina<sup>1,5</sup> , Ming Lin<sup>1</sup> , Michel Bosman<sup>1,6</sup> & Kuan Eng Johnson Goh<sup>1,2,7,8,9</sup>  

Engineering sapphire substrates with specific surface characteristics is crucial for the epitaxial growth of high-quality wafer-scale transition metal dichalcogenides, essential for integration with semiconductor industry processes. Here, we report that atomic-step-engineered sapphire surfaces undergo structural and chemical changes upon air exposure, which may be associated with surface hydrolysis and the formation of aluminum (oxy)hydroxides as revealed by a self-developed charge-contrast enhanced X-ray photoelectron spectroscopy technique. We suggest these species transform into oxygen-deficient  $\text{Al}_2\text{O}_{3-x}$  under typical growth conditions, associated with disrupted domain alignment. We further demonstrate that ultraviolet light irradiation in air appears to mitigate this degradation, restoring surface stoichiometry and promoting epitaxial alignment. The grown monolayer  $\text{WS}_2$  films exhibit high crystalline quality, good uniformity, and low defect density. Statistical analysis of 100 field-effect transistors shows a device yield >95% and a mobility variation <20%. These findings provide relevant insights for the consistent production of industrial-scale, high-quality 2D semiconductors.

The scalable epitaxy of single-crystal two-dimensional (2D) transition metal dichalcogenides (TMDs) on insulating substrates that are compatible with semiconductor industry will enable the mass production of next-generation 2D electronics based on TMDs<sup>1–6</sup>. Among various growth substrates, c-plane sapphire has emerged as a promising option for TMD epitaxy due to its crystallographic compatibility and its chemical and thermal resilience under typical growth conditions<sup>7,8</sup>. In the past few years, significant advances have been made in wafer-scale single-crystal TMD synthesis through strategic engineering of the sapphire surface. This includes optimizing miscut orientation towards the a-axis<sup>8</sup>, creating vicinal a-plane surfaces<sup>9</sup>, developing immature

step edges for enhanced nucleation<sup>10</sup>, reconstructing for single atomic plane exposure<sup>7</sup>, and modulating the surface chemistry through controlled growth conditions<sup>11</sup>.

Sapphire has the  $\alpha$ -phase hexagonal lattice structure, with in-plane unit cell dimensions  $a = b = 4.76 \text{ \AA}$  and an out-of-plane dimension  $c = 12.996 \text{ \AA}$ , characterized by six layers of alternating Al–O–Al atoms terminating in Al<sup>12–15</sup>. The normal termination of clean  $\alpha$ - $\text{Al}_2\text{O}_3$  consists of one Al atom for every three O atoms, with the terminal Al above the plane of the close-packed O<sup>16</sup>. Surface atomic features, such as step terrace terminations and step edges orientation have been utilized to modulate the coupling interaction between TMD crystals and a

A full list of affiliations appears at the end of the paper.  e-mail: [fu\\_wei@imre.a-star.edu.sg](mailto:fu_wei@imre.a-star.edu.sg); [kejgoh@yahoo.com](mailto:kejgoh@yahoo.com)

suitably engineered sapphire substrate for achieving well-resolved domain alignment during epitaxial growth<sup>7,8,10,17</sup>. However, in most conventional processes, engineered sapphire substrates are inevitably exposed to air, which may introduce variability in the epitaxial growth. Reports on the structural changes of engineered sapphire exposed to air and its impact on subsequent epitaxial growth remain limited. The  $\alpha$ - $\text{Al}_2\text{O}_3$  surface has been shown to react with  $\text{H}_2\text{O}$  to form aluminum (oxy)hydroxide in carefully controlled experimental as well as theoretical studies<sup>18–22</sup>. During the thermal heating at temperatures ranging from 700 °C to 1000 °C, similar to those of typical epitaxial growth conditions, the pyrolysis of aluminum (oxy)hydroxide occurs resulting in oxygen vacancy-rich  $\text{Al}_2\text{O}_{3-x}$ <sup>23,24</sup>. This process changes the surface chemistry and can significantly impact the alignment of crystal domains during epitaxy. A complete understanding of the atomic step engineered sapphire surface degradation mechanism upon exposure to air, and strategies for limiting/repairing this degradation, are crucial for achieving consistent, high-quality TMD epitaxy.

Here, we report a systematic study of the impact of air exposure on the surface chemistry of sapphire substrates and the consequence on the domain orientation of a prototypical 2D monolayer- $\text{WS}_2$ . By developing a charge-contrast enhanced XPS surface analysis capability, we found significant changes in the surface chemistry of atomic-step-engineered sapphire when exposed to air, which reduced domain alignment during epitaxial growth of the  $\text{WS}_2$  monolayers by chemical vapor deposition (CVD), as illustrated in Fig. 1a. Our characterization

suggests that air exposure may lead to surface hydrolysis, forming aluminum (oxy)hydroxide, as shown in Fig. 1b, which can subsequently decompose into oxygen-deficient  $\text{Al}_2\text{O}_{3-x}$  during CVD growth conditions. This altered surface chemistry appears to adversely compromise the  $\text{WS}_2$  domain orientation. We also found that larger atomic-step heights accelerate this surface transformation. Notably, our experiments suggest that UV light irradiation of air-exposed sapphire surfaces effectively removes the hydroxyl groups and restores the degraded sapphire surface to crystalline  $\alpha$ - $\text{Al}_2\text{O}_3$  during the growth stage. Our findings of deactivation of sapphire by air exposure and its subsequent restoration through UV irradiation provide valuable insights for the commercial production of high-quality 2D semiconductors.

## Results and Discussion

### Air-induced surface hydrolysis on engineered sapphire

We selected the commercially available and commonly used c-plane sapphire, cleaved along  $\mathbf{a} \langle 11\bar{2}0 \rangle$  direction as our model substrate. Through a custom thermal annealing process (see details in experimental section), the sapphire surface was engineered with atomic steps along  $\mathbf{m} \langle 10\bar{1}0 \rangle$  orientation and terminated of half-Al surfaces (see Supplementary Fig. 1). The surface profile of the freshly annealed sapphire measured by atomic force microscopy (AFM), is shown in Figs. 1c and S2 (see Supplementary Note 1). These images display a regular and uniform arrangement of surface atomic steps along the  $\mathbf{m} \langle 10\bar{1}0 \rangle$  direction with step height of  $\sim 0.25$  nm (line profile, as shown

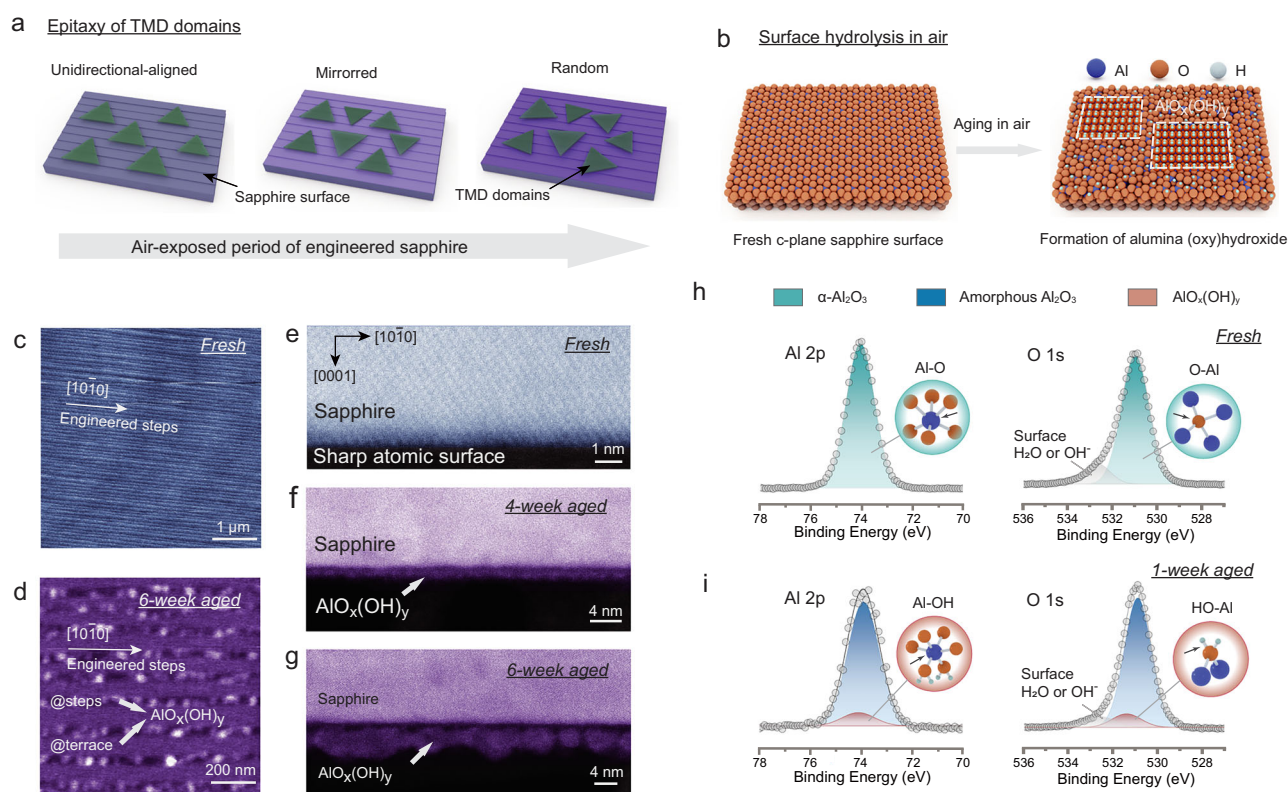


**Fig. 1 | Air-induced surface evolution on engineered sapphire.** **a** Schematic illustrating the surface structural changes of c-plane sapphire ( $\alpha$ - $\text{Al}_2\text{O}_3$ ) during air exposure and its impact on domain orientation of epitaxy. **b** Schematic of the formation of aluminum (oxy)hydroxide on sapphire surface during the air exposure. Blue spheres represent Al atoms, red spheres represent O atoms, white spheres represent H atoms. **c** The atomic force microscopy (AFM) image of freshly annealed sapphire with atomic steps towards  $\mathbf{m} \langle 10\bar{1}0 \rangle$  direction. **d** AFM image of sapphire, air exposed for 6 weeks, displaying additional cluster formation along atomic steps, which indicates preferential hydrolysis at these locations. **e–g** Cross-section scanning transmission electron microscope (STEM) images of sapphire

surfaces (on the terraces) after freshly annealing and aging in air for 4 and 6 weeks, viewed from the  $\langle 11\bar{2}0 \rangle$  direction, revealing a crystalline atomic resolved surface on freshly annealed sapphire and the development of amorphous layers during air exposure. **h, i**, High-resolution Al 2p and O 1s X-ray photoelectron spectroscopy (XPS) spectra of freshly annealed and 1-week-aged sapphire samples under high low-energy electron flux settings, identifying the characteristic Al-O bonding spectra of  $\alpha$ - $\text{Al}_2\text{O}_3$  in freshly annealed sapphire, and spectral shape change becoming detectable by XPS evidenced by additional Al-OH bonding peaks of aluminum (oxy)hydroxide likely arising from surface hydrolysis, as elucidated through XPS peak deconvolution for the 1-week aged sapphire sample.

in Supplementary Fig. 2c). The Fig. 1e shows the cross-section scanning transmission electron microscope (STEM) image of freshly annealed sapphire, viewed from a  $\langle 1\bar{1}20 \rangle$  direction, exhibiting the sharp atomic profile on surface<sup>8</sup>.

To elucidate the structural transformations of sapphire surfaces exposed to air, freshly engineered sapphire samples were aged in a cleanroom environment (class 10 K, 45% humidity) for varying durations. Figure 1d is an AFM image of the sapphire surface after aging for 6 weeks, showing the formation of distinct clusters along the edges of atomic surface steps and uniform film on the terraces. Previous work noted that surface hydrolysis can occur on the sapphire surfaces when exposed to humid air<sup>18</sup>. Assuming that these clusters are the product of that hydrolysis, our observation could indicate that hydrolysis preferentially targets the engineered atomic step edges of sapphire. In contrast, the AFM images of sapphire aged for shorter periods of 1–2 weeks (see Supplementary Fig. 3) show no discernible morphological changes, indicating that the early-stage structural transformations were not detectable at the sensitivity level of the AFM system used. To detect these early-stage changes, we therefore used cross-sectional STEM analysis of sapphire surfaces aged for 2, 4, and 6 weeks, respectively. Cross-sectional STEM images viewed along the  $\langle 1\bar{1}20 \rangle$  direction (Fig. 1e–g) illustrate the main morphological evolution of the sapphire surface upon air exposure, transitioning from a freshly annealed state to one aged for six weeks. The formation of an amorphous surface layer is evident, with a thickness ranging from 1 to 4 nm. Additional cross-sectional imaging of the two-week air-exposed sapphire along the  $\langle 10\bar{1}0 \rangle$  direction (see Supplementary Fig. 4) reveals a continuous amorphous layer enveloping both terrace and steps of the sapphire surface. A more detailed chronological sequence is shown in Supplementary Fig. 5 together with a schematic of the morphological evolution of the sapphire surface under air exposure depicted in Supplementary Fig. 6. This evolution involves the initial structural transformation of an amorphous layer on the atomic step edges, which is subsequently followed by the formation of cluster particles during the surface hydrolysis.

The XPS was employed to elucidate the impact of air exposure on the surface chemistry of engineered sapphire. Considering that sapphire is an insulator, it may accumulate a net positive charge due to photoelectron loss when subjected to X-ray irradiation<sup>25</sup>. To counteract this, a low-voltage electron flood gun was utilized to provide charge compensation by directing an electron beam onto the surface. The electron flux intensity was regulated by adjusting the filament current of the electron flood gun. The adventitious carbon C 1s spectrum is recorded and used as internal reference for bias-referencing<sup>25</sup>. High electron flux intensity settings (detailed in Supplementary Table 1) were used to analyze the Al 2p and O 1s XPS spectra of both freshly annealed and 1-week aged sapphire, shown in Fig. 1h, i, respectively, along with the peak fitting results in Supplementary Table 2. The high-resolution Al 2p and O 1s spectra of freshly annealed sapphire (Fig. 1h and Supplementary Fig. 7) revealed an Al 2p peak at 74.1 eV and a primary O 1s peak at 531 eV, indicative of O–Al–O bonding in the  $\alpha$ -Al<sub>2</sub>O<sub>3</sub><sup>26</sup>. An additional O 1s peak at 532.4 eV was observed, attributed to physically adsorbed H<sub>2</sub>O or dissociated OH<sup>-</sup> radicals on the surface<sup>27</sup>. After 1 week of air exposure, peak deconvolution of the Al 2p and O 1s spectra (Fig. 1i) revealed the emergence of additional Al–OH bonding peaks, located at 531.4 eV for O 1s and 74.1 eV for Al 2p, attributed to the formation of hydrolysis-induced aluminum (oxy)hydroxide<sup>26</sup>. The slight shifts in Al 2p and O 1s binding energies between the sapphire and its hydrolyzed phases, similar to gibbsite and boehmite (see Supplementary Fig. 8), are minimal around 0.1–0.4 eV (in Supplementary Table 2), closely approaching the resolution limits of XPS, which poses challenges for analysis.

### Charge-contrast enhanced XPS analysis of the surface changes

Given that the hydrolyzed phase preferentially accumulates at atomic step edges of engineered sapphire, as observed in the AFM image in

Fig. 1d, and considering the higher dielectric constant of hydrolyzed AlO<sub>x</sub>(OH)<sub>y</sub> compared to that of crystalline sapphire due to increased porosity and hydroxyl content<sup>28</sup>, we developed a charge-contrast enhanced XPS technique to improve the detection resolution between the two surface phases. The experimental setup, shown in Fig. 2a, incorporates a low-energy electron flood gun, which modulates the surface potential of the sample by adjusting the electron flux via control of the filament current. As illustrated in Fig. 2b, increasing the electron flux induces a series of charging regimes at the surface: (i) a net positive potential when the electron supply is insufficient to compensate for photoelectron loss; (ii) a near-neutral transition region; and (iii) a net negative potential when electrons are in excess, resulting in surface overcompensation.

The corresponding energy band diagrams are shown in Fig. 2c. Under low or no electron flux (i), both the  $\alpha$ -Al<sub>2</sub>O<sub>3</sub> and AlO<sub>x</sub>(OH)<sub>y</sub> phases exhibit similar, relatively large positive surface potentials ( $V_s^{\text{AlO}_x(\text{OH})_y} \approx V_s^{\alpha\text{-Al}_2\text{O}_3}$ ), leading to collective shifts of the O 1s and Al 2p peaks toward higher binding energies, without discernible differential shifts between the two phases. At moderate electron flux (ii), the overall surface potential becomes nearly charge neutral. However, due to spatial inhomogeneity in charge compensation, excess electrons preferentially accumulate in the hydrolyzed AlO<sub>x</sub>(OH)<sub>y</sub> domains, producing a larger local negative potential ( $V_s^{\text{AlO}_x(\text{OH})_y} > V_s^{\alpha\text{-Al}_2\text{O}_3}$ ). This charge-contrast effect enhances the differential surface potentials, resulting in a pronounced increase in the differential peak shifts ( $\Delta B$ ) between Al–O @ Al<sub>2</sub>O<sub>3</sub> and Al–OH @ AlO<sub>x</sub>(OH)<sub>y</sub> of the two phases ( $\Delta B' > \Delta B$ ), thereby significantly improving phase resolution and spectral distinction. At high electron flux (iii), the overcompensation forces the potential to become less contrasting across the surface, minimizing potential differences ( $V_s^{\text{AlO}_x(\text{OH})_y} \approx V_s^{\alpha\text{-Al}_2\text{O}_3}$ ), and the differential peak shifts becomes unresolvable.

To experimentally modulate the sample surface potential, we varied the filament current of the electron flood gun, establishing three charge-control modes: no electron flux (NEF, mode i), moderate electron flux (MEF, mode ii), and high electron flux (HEF, mode iii), with detailed settings provided in Supplementary Table S1. The C 1s peak from the adventitious carbon layer was used as an internal charge reference, with the charge-neutral position defined at 284.8 eV, consistent with typical values between 284.6–285.2 eV<sup>25</sup>. As shown in Fig. 2d, in the absence of electron flux (NEF), the C 1s peak is shifted markedly to 306.5 eV, indicating a strong positive surface potential and a shift of +21.7 eV. Under MEF conditions (20  $\mu\text{A}/\text{cm}^2$ ), the C 1s peak aligns at 284.6 eV, confirming near-neutral surface potential. In HEF mode (24  $\mu\text{A}/\text{cm}^2$ ), the C 1s peak shifts to 282.6 eV, suggesting a negatively biased surface due to electron overcompensation.

We first examined freshly annealed sapphire under all three flux conditions. Angle-resolved XPS spectra of Al 2p, O 1s, and C 1s showed no evidence of differential charging, confirming that the system was properly configured and that charging artifacts were not present (see Supplementary Note 2, Supplementary Figs. 9–11, Supplementary Table 3).

After two weeks of ambient air exposure, XPS survey scans of the sapphire surface (see Supplementary Fig. 12) detected only aluminum, oxygen, and adventitious carbon, confirming the absence of extrinsic surface contaminants. To probe the evolution of surface chemistry, angle-resolved high-resolution spectra were collected under three distinct charge compensation conditions—no electron flux (NEF), moderate electron flux (MEF), and high electron flux (HEF)—as detailed in Supplementary Note 3, Supplementary Figs. 13–21 and Supplementary Tables 4–7. Representative spectra acquired at a 30° take-off angle are shown in Fig. 2e. Under MEF conditions, the binding energies corresponding to Al–O bonding in bulk  $\alpha$ -Al<sub>2</sub>O<sub>3</sub> appear at 530.8 eV (O 1s) and 73.9 eV (Al 2p), in good agreement with those observed in HEF mode. Notably, additional low-binding-energy shoulders are observed at 529.0 eV (O 1s) and 72.3 eV (Al 2p), with their relative

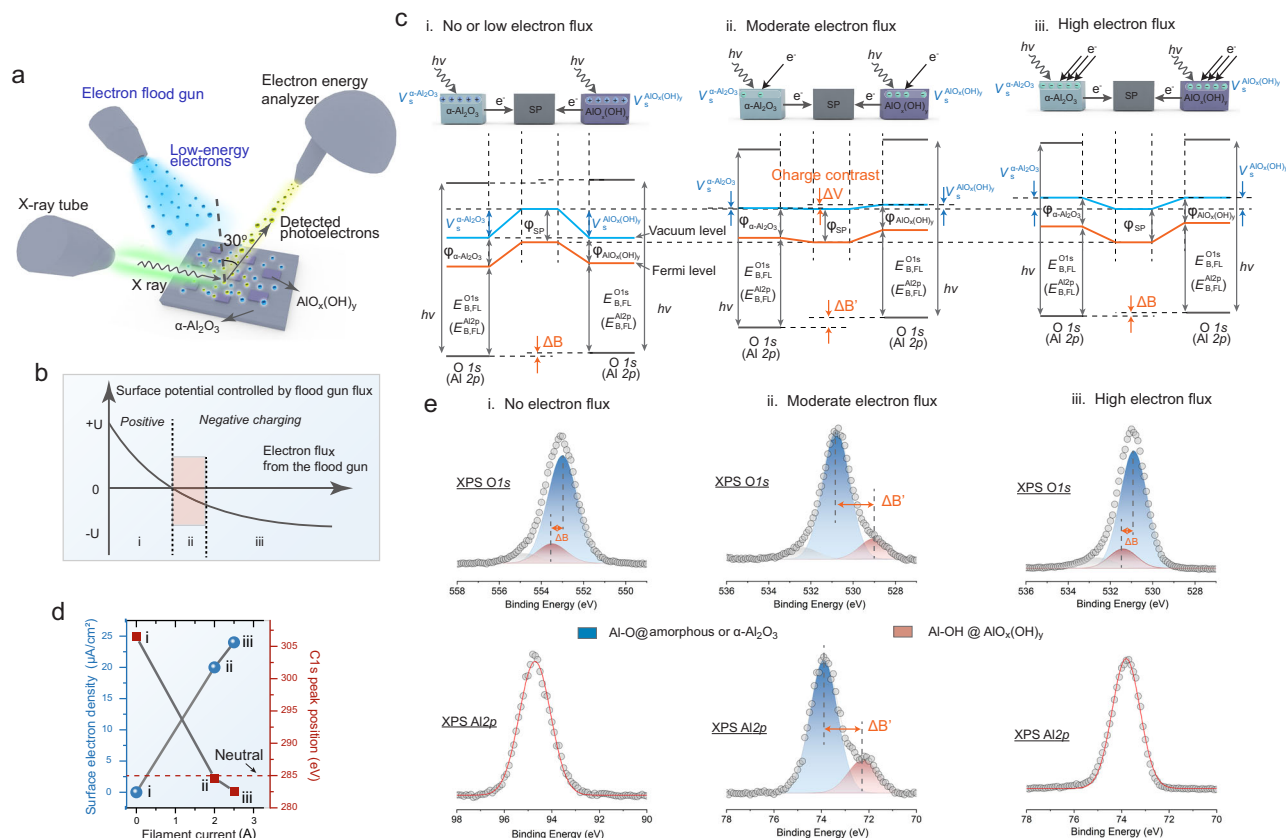


**Fig. 2 | Charge-contrast enhanced XPS analysis of engineered sapphire surface changes upon air aging.** **a** Schematic of the XPS setup equipped with an electron flood gun, which emits low-energy electrons to control the surface charging. **b** Illustration of surface potential modulation as a function of incident electron flux: (i) net positive charging (+U), (ii) near-neutralization, and (iii) overcompensation leading to net negative charging (-U). **c** Corresponding energy level alignments at the sample-spectrometer (SP) interface during under different charging conditions.  $h\nu$  is the energy of the incident radiation.  $e^-$  means emitted electrons.  $V_s$  is the surface potential.  $\phi$  is the work function.  $E_{B,FL}$  is the binding energy referenced to the Fermi level (FL).  $\Delta B$  and  $\Delta B'$  are the differential peak shifts between Al-O @  $\text{Al}_2\text{O}_3$  and Al-OH @  $\text{AlO}_x(\text{OH})_y$  without and with surface charge differential contrast ( $\Delta V$ ). At no or low electron flux (i), uncompensated photoemission results in a net

positive surface potential and core-level shifts toward higher binding energies. At moderate flux (ii), partial neutralization occurs, and excess electrons accumulate in surficial  $\text{Al}_2\text{O}_3$  and  $\text{AlO}_x(\text{OH})_y$  domains. This induces localized differential charging, enhancing both the O 1s and Al 2p peak separations between the two surface phases. At high flux (iii), excess electrons create a generally less contrasting negative surface potential. **d** Relationship between flood gun filament current and resulting electron flux, correlated with C 1s peak positions used for charge referencing. **e** Al 2p and O 1s spectra of engineered sapphire after 2 weeks of air aging, acquired under different electron flood gun settings. The charge-contrast effect amplifies the binding energy differences between two surface phases, with the Al-OH bonding energy reduced by 1.5 eV, thereby enabling unambiguous phase differentiation via increased peak separation in both O 1s and Al 2p spectra.

intensities increasing at shallower detection angles, suggesting a surface-enriched phase. These spectral features, coupled with AFM and cross-sectional STEM results, indicate hydrolytic transformation of the surface upon air exposure and the formation of a surficial aluminum (oxy)hydroxide layer. We thus attribute the shoulder peaks to Al-OH bonding within the hydrolyzed  $\text{AlO}_x(\text{OH})_y$  domains.

Quantitative fitting reveals a consistent O 1s peak area ratio of Al-O to Al-OH of -0.167 across all modes. Notably, the Al-OH-related O 1s and Al 2p peaks shift from 531.1 eV and 74.1 eV (HEF) to 529.0 eV and 72.3 eV (MEF), respectively—downshifts of 2.1 eV and 1.8 eV. These enhanced chemical shifts are attributed to the charge-contrast effect, which increases the differential surface potentials between  $\alpha\text{-Al}_2\text{O}_3$  and  $\text{AlO}_x(\text{OH})_y$  phases, thereby amplifying the binding energy separation and improving phase resolution in the XPS spectra.

The charge contrast effect under MEF mode proves to be advantageous in distinguishing the chemical structure of mixed phases on insulating surfaces that exhibit similar bonding energies. By selectively shifting the phase with higher dielectric constant to lower binding energies during the XPS measurement, this technique enhances the detection and analysis of subtle structural changes on insulating surfaces. Utilizing this approach, we investigated the air exposure-

dependent evolution of the surface phase on the sapphire and found that the sapphire surface undergoes progressive hydrolyzation into aluminium (oxy)hydroxide—from 11% in the first week to 67% after eight weeks. The detailed angle-resolved XPS spectra and a summary of the fitting are shown in Supplementary Note 4, Supplementary Fig. 22-25 and Supplementary Table 8. Furthermore, we evaluated the air-induced structural transformations on sapphire surfaces engineered with different atomic step heights of 0.2 nm and 1.0 nm and found that the higher the atomic step height on sapphire surfaces, the more pronounced the structural transforms triggered by hydrolysis. The detailed angle-resolved XPS spectra and summary of fitting are shown in Supplementary Note 5, Supplementary Figs. 26, 27 and Supplementary Table 9.

The hydrolysis of  $\alpha\text{-Al}_2\text{O}_3$  in air, resulting in the formation of amorphous  $\text{Al}_2\text{O}_3$  and  $\text{AlO}_x(\text{OH})_y$ , significantly influences the surface chemistry of  $\alpha\text{-Al}_2\text{O}_3$  during the epitaxial growth of TMD atomic layers. Typically, the epitaxial growth of TMDs occurs at temperatures ranging from 700 to 1000 °C in an oxygen-free environment<sup>11,27,29–31</sup>. This thermal heating during the growth process can substantially alter the surface structure of sapphire, thereby compromising the controllability of the epitaxy growth.

To explore the surface structural changes of aged sapphire under epitaxial growth conditions, we selected a two-week-aged sapphire sample with 21% surface coverage of  $\text{AlO}_x(\text{OH})_y$  as a model system. This sample was placed in a tube furnace and subjected to standard growth conditions, including specified temperature settings and gas flow, but without introducing growth precursors (detailed recipe in Supplementary Fig. 28). The detailed XPS analysis of pre-growth heating induced structural transformation of aged sapphire is shown in Supplementary Note 6, Supplementary Fig. 29 and Supplementary Table 10. After post-growth heating at 950 °C, the Al 2p and O 1s peaks showed a sharpening corresponding to Al-O bonding in  $\text{Al}_2\text{O}_3$ , indicative of a phase transformation from amorphous to crystalline  $\alpha\text{-Al}_2\text{O}_3$  at 950 °C, using the underlying  $\alpha\text{-Al}_2\text{O}_3$  substrate as a crystalline template<sup>32–34</sup>. Moreover, we observed the disappearance of the characteristic  $\text{AlO}_x(\text{OH})_y$  peaks (Al 2p at 72.3 eV and O 1s at 529 eV) and a significant increase in the peak area of high-energy O 1s peaks at 534.2 eV, which we attributed to surface OH<sup>-</sup> or H<sub>2</sub>O bonding<sup>23</sup>. These changes suggest the pyrolysis of the  $\text{AlO}_x(\text{OH})_y$  phase during the thermal process, leading to the formation of an oxygen-vacancy-rich  $\text{Al}_2\text{O}_{3-x}$  phase, which enhances surface H<sub>2</sub>O adsorption or hydroxylation upon air exposure during sample transfer. Previous studies indicate that heat-induced dehydroxylation of aluminium (oxy)hydroxide, such as  $\text{Al}(\text{OH})_3$ , leads to the formation of non-stoichiometric  $\text{AlO}_x$  clusters with abundant oxygen vacancies when heated between 500 °C and 1000 °C<sup>23,35,36</sup>. These oxygen vacancies on the  $\alpha\text{-Al}_2\text{O}_3$  surface can induce energetically favorable surface reconstructions, leading to the formation of various Al-rich surface structures distinct from the original crystalline  $\alpha\text{-Al}_2\text{O}_3$  surface<sup>12,13,37</sup>. The increase in the Al/O ratio from 0.57 to 0.76 before and after pre-growth heating at 950 °C, as shown in Supplementary Fig. 30, further supports the formation of an oxygen-vacancy-rich or Al-rich layer on the  $\alpha\text{-Al}_2\text{O}_3$  surface.

### Ultraviolet light healing of degraded sapphire surfaces

UV irradiation is a well-established surface cleaning method, recognized for its effectiveness in removing organic contaminants and its suitability as a dry-cleaning technique<sup>38</sup>. Previous research has shown that UV exposure significantly reduces Al-OH bonds in ALD-grown  $\text{Al}_2\text{O}_3$  through a photo-induced electron transfer process. This involves electrons moving from deeper to shallower traps, accompanied by redox reactions that disrupt and create chemical bonds<sup>39,40</sup>. Considering that the transformation of  $\alpha\text{-Al}_2\text{O}_3$  surfaces in air primarily results from the accumulation of hydroxyl-rich phases such as  $\text{AlOOH}$  or  $\text{Al}(\text{OH})_3$ , we explored the use of UV light irradiation to remove the aluminium oxyhydroxide layers from aged  $\text{Al}_2\text{O}_3$  surfaces.

To investigate the effects of UV irradiation on air-exposed sapphire substrates, we selected a sapphire sample with 2 weeks of air exposure as a model. This sample was subjected to UV irradiation (in air,  $\lambda = 320$  to 400 nm, power density of 0.5 W/cm<sup>2</sup>) for 30 min, as illustrated in Fig. 3a with the setup given in Supplementary Fig. 31. Subsequent XPS analysis, presented in Supplementary Note 7, Supplementary Fig. 32 and Supplementary Table 11, revealed notable structural transformations induced by UV irradiation. In Fig. 3b, we observed the disappearance of characteristic  $\text{AlO}_x(\text{OH})_y$  peaks at Al 2p 72.3 eV and O 1s 529 eV, alongside a notable broadening at Al 2p 74 eV and O 1s 531 eV, corresponding to Al-O bonding in  $\text{Al}_2\text{O}_3$ . These changes suggest a transformation into an amorphous  $\text{Al}_2\text{O}_3$  phase. These results confirm that UV light irradiation effectively decomposes the surface  $\text{AlO}_x(\text{OH})_y$  phase into amorphous  $\text{Al}_2\text{O}_3$ , as depicted in Fig. 3a.

To investigate the surface transformation of the above UV irradiated sample under growth, we put that sample in the pre-growth heating process. In Fig. 3b, the Al 2p and O 1s peaks after this pre-growth heating exhibited a noticeable sharpening, with the full width at half maximum (FWHM) reduced to 1.19 and 1.25 eV, respectively, closely matching the 1.15 and 1.22 eV observed in freshly annealed

sapphire. The UV irradiated sample displayed a much weaker peak, in contrast with the prominent O 1s peak at 523.4 eV that is typically associated with OH<sup>-</sup> or H<sub>2</sub>O bonding and indicative of rich oxygen vacancies in the sapphire sample after pre-growth heating of 2-week aged sapphire without UV irradiation. This suggests a reduction in oxygen vacancies for the UV irradiated sample, aligning the spectra characteristics more closely with those of freshly annealed sapphire. As illustrated in Fig. 3a, UV irradiation before the growth process significantly restores the surface of degraded sapphire by removing  $\text{AlO}_x(\text{OH})_y$ , reverting it to a structure similar to that of freshly annealed sapphire in the pre-growth process. This restoration is further supported by the Reflection High-Energy Electron Diffraction (RHEED) diffraction patterns of the 2-week-aged sapphire and the repaired sapphire after 2-week aging, UV irradiation, and pre-growth heating process. In Fig. 3c, the aged  $\text{Al}_2\text{O}_3$  sample initially shows a bright background with a blurred diffraction pattern, indicative of an amorphous layer on the  $\alpha\text{-Al}_2\text{O}_3$  surface<sup>41</sup>. In contrast, following UV exposure and pre-growth heating, the sample displays distinct and sharp RHEED stripes characteristic of crystalline  $\alpha\text{-Al}_2\text{O}_3$ , as confirmed by the intensity profile comparison in Fig. 3d. The RHEED pattern of the repaired sapphire closely matches that of freshly annealed sapphire (in Supplementary Fig. 33), providing evidence of effectiveness of UV light in restoring the degradation of the sapphire surface.

### Domain orientation evolution

Our investigation into the surface chemistry of sapphire under air exposure reveals that, after air exposure without UV irradiation, the sapphire surface exhibits a significant presence of oxygen vacancies: i.e. an Al-rich layer on the  $\alpha\text{-Al}_2\text{O}_3$  surface. We hypothesize that the balance between strain in the Al-rich adlayer and the preference for Al atoms to occupy specific sites on the  $\alpha\text{-Al}_2\text{O}_3$  substrate drives the formation of a  $\sqrt{31} \times \sqrt{31}$  R9°- $\text{Al}_2\text{O}_3$  (0001) surface, consisting of a single well-ordered overlayer of surface Al atoms on bulk  $\text{Al}_2\text{O}_3$ <sup>42</sup>.

As illustrated in Figure S34, the  $\sqrt{31} \times \sqrt{31}$  R9° reconstruction emerges from a relaxed (1×1) surface by desorbing the top two O layers along with a fraction of the surface Al<sup>43</sup>. This reconstruction typically forms under ultra-high vacuum annealing at temperatures above 1400 °C<sup>12,44</sup> or by depositing 1 monolayer of Al atoms on  $\alpha\text{-Al}_2\text{O}_3$  at lower temperature, such as 800 °C<sup>45,46</sup>. The formation of the  $\sqrt{31} \times \sqrt{31}$  R9° structure is influenced by the balance between the surface oxygen vacancies density and the temperature. Specifically, at low temperatures of 800 °C with high oxygen depletion (11%, calculated from the structure model of one monolayer Al deposited on  $\alpha\text{-Al}_2\text{O}_3$  surface) and at high temperatures 1450 °C with low oxygen depletion (2%<sup>47</sup>) the  $\sqrt{31} \times \sqrt{31}$  R9° reconstruction can form. In our experiment, the combination of high oxygen depletion and a high growth temperature of 950 °C falls within the range that can facilitate the formation of the  $\sqrt{31} \times \sqrt{31}$  R9° reconstruction.

Additionally, we noted an increased intensity of the OH peak at 532.4 eV in O 1s spectrum post pre-growth heating, as detailed in Supplementary Fig. 29b and Supplementary Table 10. This observation, coupled with the absence of a metallic Al layer suggests the reoxidation of the Al metal layer during sample transfer likely induced by exposure to air. This observation aligns with previous research, which demonstrated that the  $\sqrt{31} \times \sqrt{31}$  R9° reconstructed structure, when exposed to water and hydrogen, forms hydroxide clusters on the surface, as evidenced by scanning force microscopy<sup>14</sup>.

To investigate the impact of the reconstructed surface structure of sapphire on the epitaxy growth of TMD, we performed DFT calculations to determine the preferential orientation of TMD on both pristine and reconstructed sapphire surfaces. In Fig. 4a, the rotating angle was defined as the anticlockwise rotation required to align the zigzag edge of the WS<sub>2</sub> triangular domain, initially parallel to the <1010> direction of the sapphire crystal, with the specific triangle. On a pristine c-plane sapphire substrate without a reconstructed Al layer,

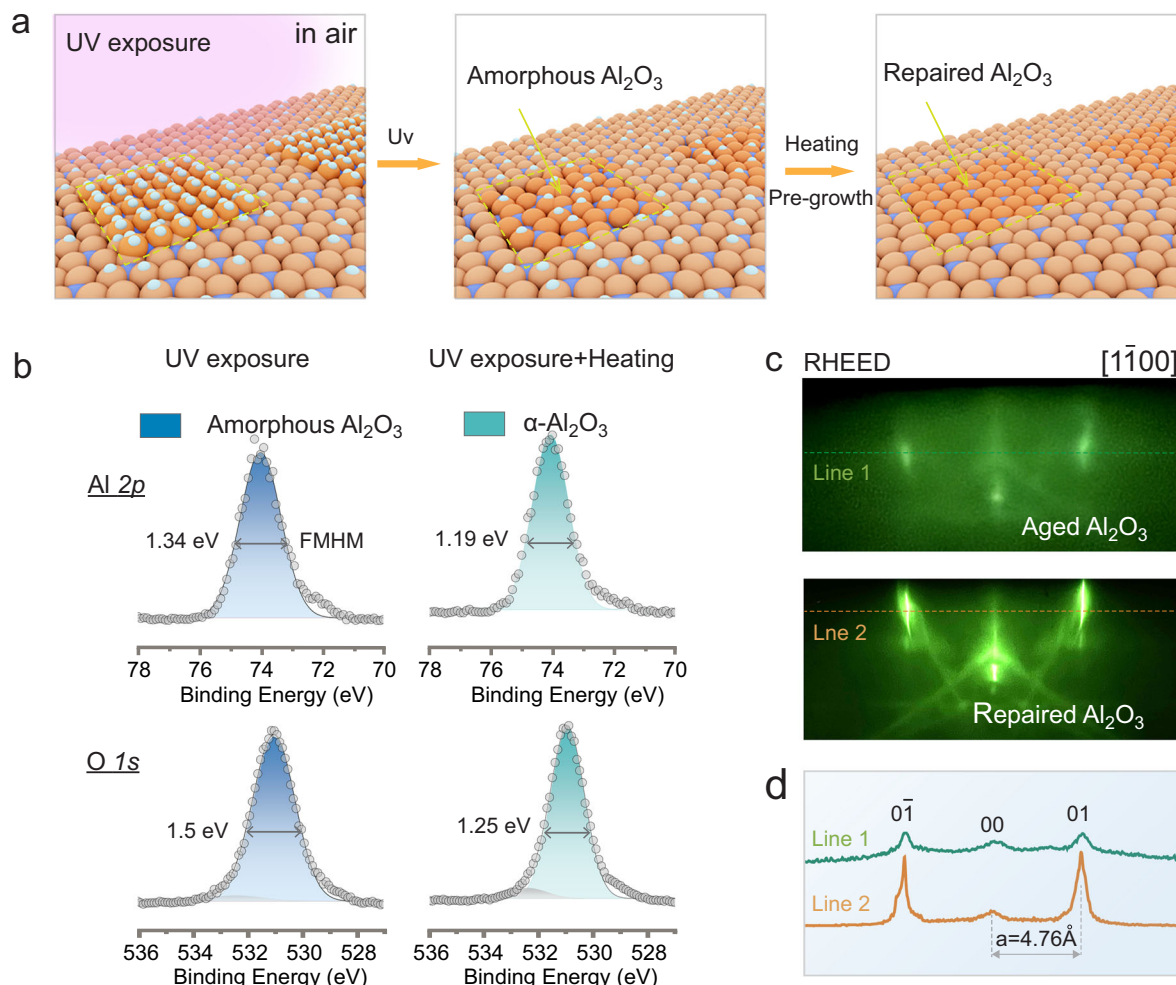


**Fig. 3 | Light irradiation repairs the surface of aged sapphire.** **a** Schematic showing ultraviolet (UV) light-irradiation-induced surface repair. **b** XPS analysis of sapphire after UV light exposure and after subsequent pre-growth heating process. The reduced full width at half maximum (FMHM) values of Al2p and O1s peaks after heating under growth conditions indicated that the sapphire appears to have

reverted to a structure similar to that of freshly annealed sapphire during the pre-growth process. **c** The reflection high-energy electron diffraction (RHEED) patterns of aged and repaired sapphires. **d** The RHEED intensity profiles recorded along the dotted lines in **c**.

mirror domains prefer orientation angles of 30° or 90°. However, with the reconstructed Al layer, the preferred orientation angles shift to 0° or 60°. The adsorption energies as a function of orientation angle, plotted in Fig. 4b, indicate that the energy-favored orientation shifts from 30° on pristine sapphire to 0° on the reconstructed Al layer. These findings suggest that surface chemistry variations play a significant role in determining the domain orientation during TMD growth.

To experimentally investigate the impact of the reconstructed Al layer on domain orientation, we used two common c-plane sapphire substrates with atomic steps along the <1120> (or a-axis) and <1010> (or m-axis) directions; the AFM analysis is given in Supplementary Fig. 35. Previous studies reported that on c-plane sapphire with <1120> atomic steps, TMD mirror domains tend to align with the step edges due to the similar degenerate energy for mirror domain nucleation<sup>48</sup>. Conversely, on c-plane sapphire with <1010> atomic steps, unidirectional domain orientation is typically observed, driven by the minimized nucleation energy induced by the step edges<sup>8</sup>. In our experiments, we employed these two sapphire substrates for the CVD growth of WS<sub>2</sub> monolayers. The stacking relationship of the domains on the sapphire crystal surface was determined by AFM. As shown in Fig. 4c, for the pristine sapphire surface with <1120> steps, mirrored domains with orientation angles of 30° and 90° were aligned along the

<1120> step edges. In contrast, on the surface with <1010> steps, unidirectional domains were observed aligned along the <1010> steps (in Supplementary Fig. 36). This observation is consistent with published research<sup>8,48</sup>, indicating that our optimized growth conditions are suitable for identifying the impact of the reconstructed Al layer on growth.

The aging-duration-dependent domain alignment is dominated by two primary factors: (1) the atomic step orientation of the c-plane sapphire substrate and (2) the degree of surface hydrolysis, which leads to the formation of aluminum (oxy)hydroxide phases (AlO<sub>x</sub>(OH)<sub>y</sub>). These two factors interact to modulate the local surface chemistry environment, thus altering the nucleation energetics of epitaxially grown WS<sub>2</sub> domains. The air-induced formation of aluminum (oxy)hydroxide and the resulting oxygen vacancies exert a profound influence on both the atomic step integrity and surface chemical environment of the sapphire substrate. By modulating the local surface potential and altering step-edge reactivity, these species act as critical regulators of domain alignment, dictating the orientation and uniformity of epitaxial growth across different step-engineered substrate configurations. The detailed discussion is in Supplementary Note 8 and Supplementary Fig. 37.

We performed a statistical analysis of domain orientation in relation to the evolution of sapphire surface chemistry over a large

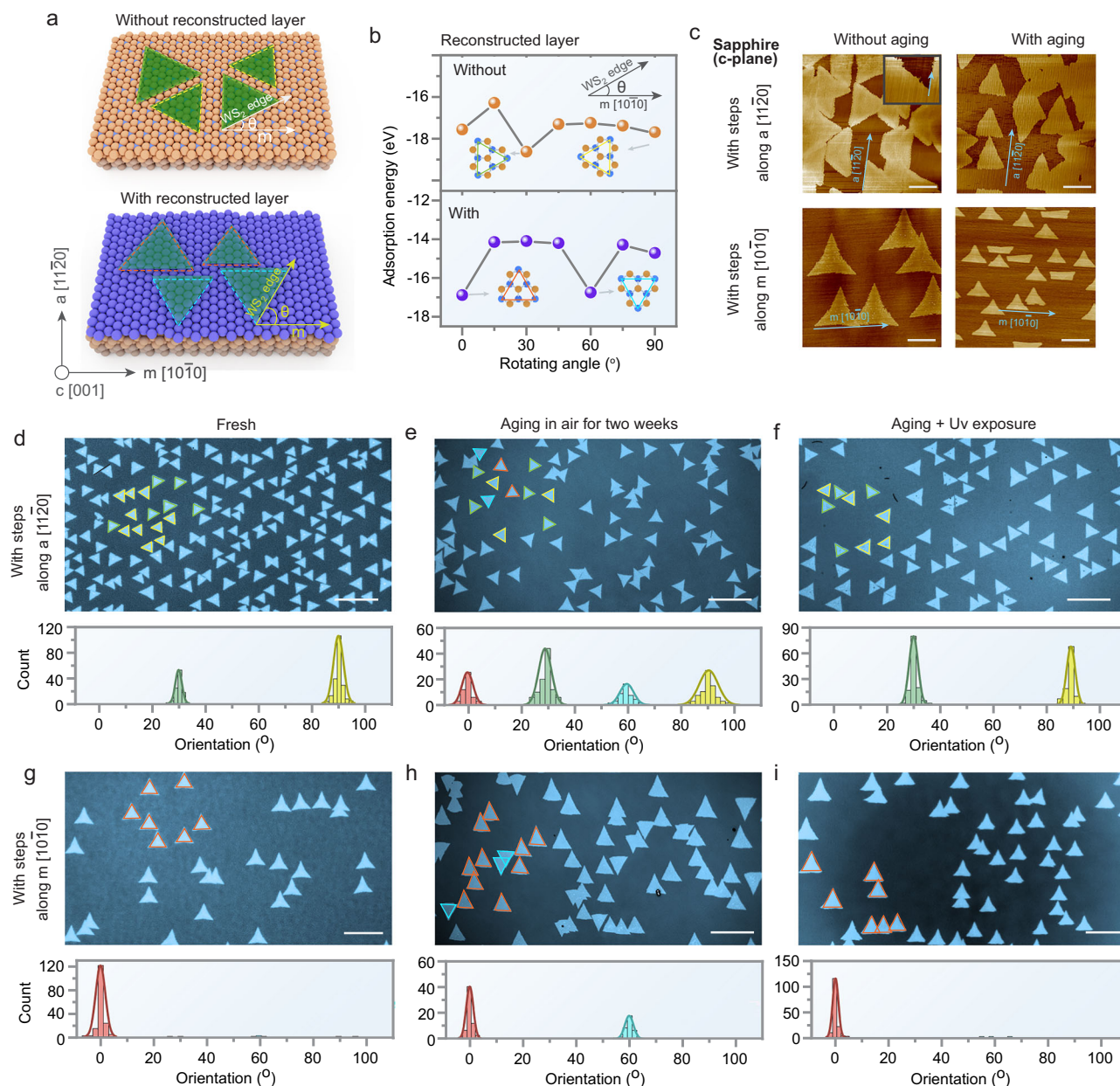


**Fig. 4 | Domain orientation during epitaxial growth of WS<sub>2</sub> monolayers.**

**a** Schematic illustration of domain orientations on sapphires with or without reconstructed Al layer. The rotating angle ( $\theta$ ) was defined as the anticlockwise rotation required to align the zigzag edge of the WS<sub>2</sub> triangular domain, initially parallel to the  $m$   $\langle 10\bar{1}0 \rangle$  direction of the sapphire crystal; **b** Calculated rotating angle-dependent adsorption energies of WS<sub>2</sub> domain attached to the sapphire surface. The insets show representative domains with different rotating angles; **c** AFM images of WS<sub>2</sub> domain orientations on sapphire substrates with atomic steps

towards  $\langle 10\bar{1}0 \rangle$  and  $\langle 1\bar{1}20 \rangle$  directions; The inset in the top-left panel provides a higher-magnification view, clearly revealing the alignment of domains along the atomic step direction towards  $\langle 1\bar{1}20 \rangle$ . Scale bars: 4  $\mu\text{m}$  (top-left, top-right, bottom-left), 1  $\mu\text{m}$  (inset of top-left and bottom-right). **d-f** The evolution of domain orientation grown on sapphire substrate with atomic steps towards the  $\langle 1\bar{1}20 \rangle$  direction; scale bars represent 20  $\mu\text{m}$ ; **g-i** The evolution of domain orientation grown on sapphire substrate with atomic steps towards the  $\langle 10\bar{1}0 \rangle$  direction, with scale bars of 10  $\mu\text{m}$ .

area. On sapphire substrates with  $\langle 1\bar{1}20 \rangle$  steps, the freshly annealed surface exhibited two mirrored domains with orientation angles of 30° and 90°, as shown in the optical image and corresponding statistical distribution of domain orientation in Fig. 4d. After two weeks of air aging, numerous additional mirrored domains with orientation angles of 0° and 60° emerged, as shown in Fig. 4e. This change is attributed to the formation of the reconstructed Al layer, derived from the aluminum oxyhydroxide precursor upon air exposure. Subsequently, when the aged sapphire was subjected to UV irradiation prior to the growth, the additional 0° and 60° domains disappeared, leaving only the original 30° and 90° domains similar to epitaxial growth observed on the

freshly annealed sapphire (Fig. 4f). We attribute this to the UV light induced healing of the degraded sapphire surface, which removes the aluminum oxyhydroxide precursor, preventing the formation of the reconstructed Al layer, and promoting the recovery of the pristine crystal surface during growth.

For sapphire with  $\langle 10\bar{1}0 \rangle$  steps, the freshly annealed surface exhibits unidirectional domain orientation at a rotating angle of 0°, as shown in the optical image and corresponding statistical distribution of domain orientation in Fig. 4g. After 2 weeks of air aging, additional domains at an orientation angle of appeared (Fig. 4h). However, following UV irradiation on the aged sapphire, no additional 60° domains

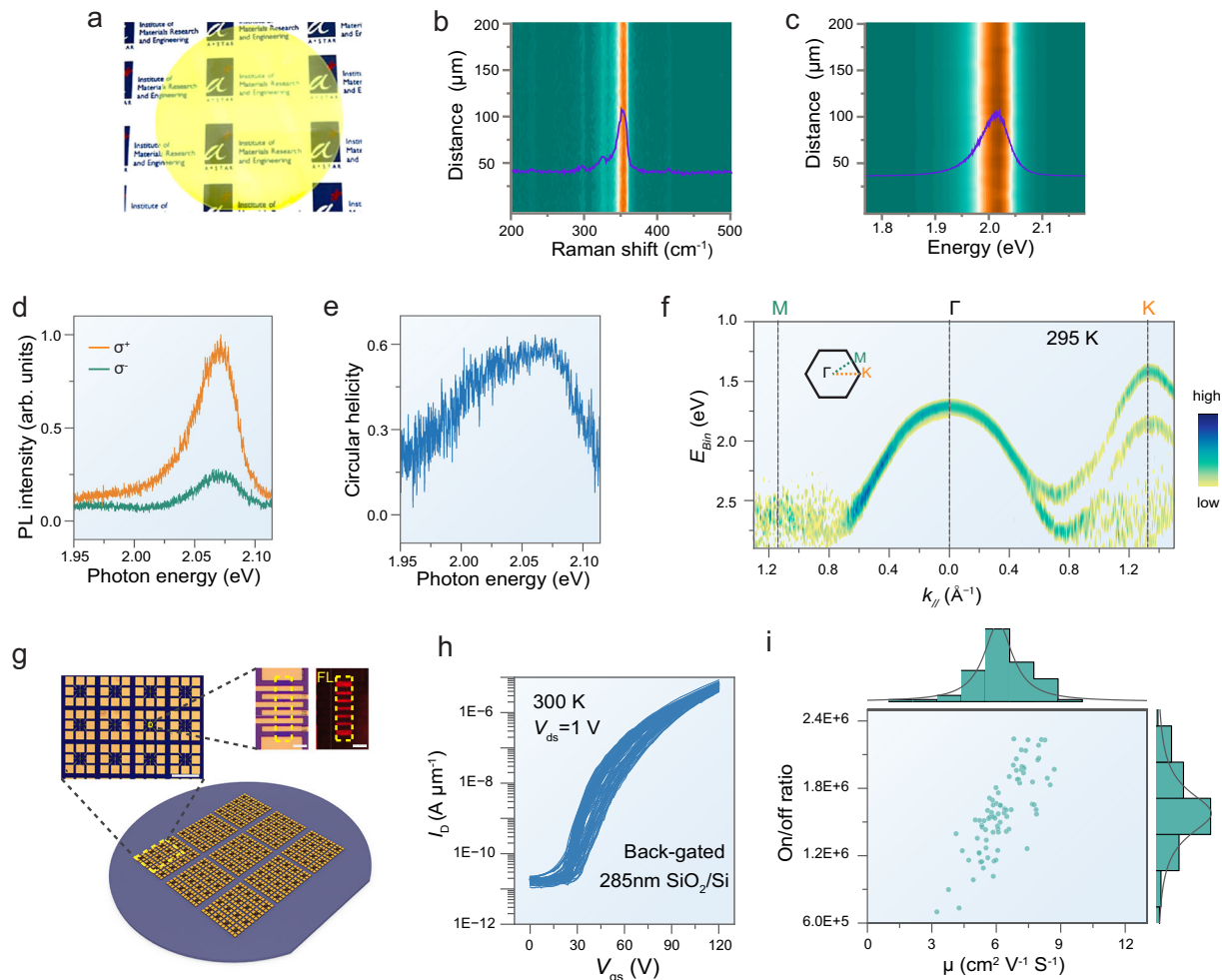


**Fig. 5 | Quality of epitaxially-grown WS<sub>2</sub> monolayer.** **a** Photograph of a 2-inch sapphire wafer with WS<sub>2</sub> monolayer film; **b** Line scan of Raman spectra at the sub-mm scale showing the uniformity of the monolayer film; **c** Line scan of photoluminescence (PL) spectra at the sub-mm scale. **d** Circular polarized PL spectra of WS<sub>2</sub> grown on c-plane sapphire with <1010> atomic steps. The excitation light is right-handed circularly polarized at 2 eV. Left-handed and right-handed circularly polarized PL spectra are shown in orange and green, respectively. **e** Circular helicity calculated from the PL spectra in **d**. The high value over 60% indicates the high quality of our WS<sub>2</sub> monolayer. **f** Experimental valence band dispersion of WS<sub>2</sub> monolayers at 295 K along the  $\Gamma$ -K point and  $\Gamma$ -M high symmetry directions of the monolayer Brillouin zone obtained from a second derivative filter of the ARPES

intensity. **g** Optical micrograph and schematic illustration of a wafer-scale array of back-gated WS<sub>2</sub> field-effect transistors (FETs). Scale bar, 400  $\mu\text{m}$ . The inset shows a zoom-in of an individual FET device and its corresponding fluorescence image (FL), confirming continuous monolayer channels. Scale bar, 5  $\mu\text{m}$ . **h** Representative transfer characteristics ( $I_D$ - $V_{gs}$ ) of 100 WS<sub>2</sub> FETs at 300 K, showing consistent n-type switching behavior with up to 6 orders of magnitudes in current change. Device yield exceeded 95%. **i**, Statistical distribution of field-effect mobility ( $\mu$ ) and on/off ratio extracted from the transport data in (**h**). A strong positive correlation can be observed between mobility and on/off ratio, with an average mobility of  $6.3 \text{ cm}^2 \text{ V}^{-1} \text{ s}^{-1}$  and an average on/off ratio of  $1.6 \times 10^6$ .

were detected, and the domains remained unidirectionally aligned with an orientation angle of  $0^\circ$  (Fig. 4i).

This result demonstrates that the evolution of sapphire surface chemistry significantly impacts the orientation of epitaxially grown domains. The formation of aluminum oxyhydroxide during air exposure leads to the emergence of a reconstructed Al layer on the pristine sapphire substrate, which compromises the epitaxial film by introducing additional domain orientations. However, UV irradiation prior to growth effectively removes this aluminum oxyhydroxide precursor, restoring the sapphire surface to a state comparable to that of a freshly annealed surface. This process recovers the original domain alignment, ensuring high-quality WS<sub>2</sub> growth.

### Quality of epitaxially-grown WS<sub>2</sub> monolayers

The UV light surface repair strategy can be applied for wafer-scale growth of WS<sub>2</sub>. A photograph of a 2-inch c-plane sapphire wafer with a WS<sub>2</sub> film shown in Fig. 5a, showing a uniform film color that indicates

consistent growth with high coverage. Optical images taken from different locations on the 2-inch WS<sub>2</sub> film confirm its high surface quality and uniformity (in Supplementary Fig. 38). Figure 5b, c present photoluminescence (PL) and Raman mapping across a 200  $\mu\text{m}$  length of the 2-inch WS<sub>2</sub> wafer, revealing no significant variations in peak position and linewidth. Furthermore, the quality of the WS<sub>2</sub> film was assessed using circularly polarized PL spectra, as shown in Fig. 5d. The calculated photon energy-dependent circular helicity in Fig. 5e indicates a very high degree of circular helicity. This serves as strong evidence of the high quality of the film, as circular helicity arises from the valley selective spin excitations at the K and K' points of the Brillouin zone of monolayer WS<sub>2</sub> and is highly sensitive to defects that introduce intervalley scattering which degrades the circular helicity. For high-quality WS<sub>2</sub> monolayer flakes exfoliated from bulk single crystals, the measured circular helicity is typically lower than 40%. Remarkably, our WS<sub>2</sub> film on sapphire exhibited circular helicity up to 60% (Fig. 5e), which is comparable to the highest reported for exfoliated flakes<sup>49,50</sup>.

Additionally, high-resolution HAADF STEM demonstrates the uniform local atomic structure of the WS<sub>2</sub> monolayer, as shown in the atomic image in Supplementary Fig. 39, the featured atomic structure with a hexagonal unit cell is clearly visible in the enlarged inset on the left.

To further assess the sample quality, the chemical composition and electronic band structure of the WS<sub>2</sub> monolayer film were measured by XPS and angle-resolved photoemission spectroscopy (ARPES). XPS data in Supplementary Fig. 40 indicate a WS<sub>2</sub> stoichiometry comparable with a WS<sub>2</sub> bulk single crystal (from HQ graphene). The valence band dispersion along the  $\Gamma$ M and  $\Gamma$ K high symmetrical directions of the Surface Brillouin Zone of the WS<sub>2</sub> monolayer is shown in Fig. 5f and Supplementary Fig. 41. The results are in line with previous measurements obtained for single crystal WS<sub>2</sub> monolayers<sup>51</sup> and confirm the single orientation of the WS<sub>2</sub> domain in the probed area (~1 mm<sup>2</sup>). For multiple domain TMD films, the simultaneous observation of GK and GM band dispersion would be expected, reflecting the different in-plane orientation of the TMD domains under the ARPES probe area, as previously reported for MoS<sub>2</sub> and WS<sub>2</sub> thin films<sup>52,53</sup>; this multiple domain signal is not observed in our WS<sub>2</sub>, emphasizing its high level of mono-crystallinity.

To evaluate the electronic quality of epitaxially grown WS<sub>2</sub> films, we first transferred the as-grown monolayers from sapphire substrates onto 285 nm SiO<sub>2</sub>/Si(p++) wafers using a PPC-assisted transfer process. As shown in Supplementary Fig. 42, the optical and fluorescence (FL) images of the transferred films reveal a uniform and continuous monolayer coverage over large areas. The films exhibit minimal cracks and wrinkles, with strong and spatially homogeneous photoluminescence intensity across the entire area, confirming the high transfer fidelity and structural integrity of the monolayer WS<sub>2</sub>, which is suitable for device integration. Furthermore, we subsequently fabricated a large-area array of global back-gated field-effect transistors (FETs) (Fig. 5g). The device layout covers a cm-scale area and is patterned uniformly across the substrate. The FL image acquired post-fabrication further verifies that the channel region maintains monolayer continuity and optical uniformity after device processing, ensuring reliable electrical characterization.

To investigate the intrinsic transport characteristics, we measured both output and transfer curves of representative devices (see Supplementary Fig. 43). The  $I_{ds}$ - $V_{ds}$  output characteristics exhibit linear behavior at low drain bias, confirming good ohmic contact between the WS<sub>2</sub> channel and metal electrodes. As the gate bias increases, the curves show pronounced nonlinearity, indicative of efficient gate modulation and enhanced carrier injection. Transfer curves acquired at varying drain biases display clear n-type field-effect behavior with current modulation spanning up to 6 orders of magnitude. The progressive increase in transconductance with  $V_{ds}$  reflects improved field-effect response under higher bias conditions. Furthermore, Fig. 5h shows the transfer characteristics of 100 devices measured at  $V_{ds} = 1$  V. The majority of devices exhibit uniform gate modulation and well-defined switching behavior. Based on the criterion of an on/off ratio exceeding 10<sup>5</sup>, we estimate a device yield of 95.6%, highlighting the excellent uniformity and reproducibility of the transferred WS<sub>2</sub> films and subsequent device fabrication process. A statistical analysis of the field-effect mobility and on/off ratio is presented in Fig. 5i. The extracted mobilities ( $\mu$ ) follow a near-Gaussian distribution with an average value of 6.27 cm<sup>2</sup> V<sup>-1</sup> s<sup>-1</sup> and a standard deviation of 1.24 cm<sup>2</sup> V<sup>-1</sup> s<sup>-1</sup>, corresponding to a 19.8% variation. The on/off ratios range from approximately 6 × 10<sup>5</sup> to 2.4 × 10<sup>6</sup>, and exhibit a strong positive correlation with mobility, suggesting that both contact resistance and interface scattering are reasonably consistent across the array.

It is worth noting that despite the high device uniformity, the mobility values remain moderate and no current saturation is observed in the output characteristics up to  $V_{ds} = \pm 2$  V (see Supplementary Fig. 43a). These observations are attributed to the use of a

global back-gate configuration with a thick 285 nm SiO<sub>2</sub> dielectric, which imposes a large equivalent oxide thickness (EOT) and thus weak gate electrostatic coupling<sup>54,55</sup>. Additionally, the lack of current saturation may arise from velocity-limited transport and long-channel effects in monolayer WS<sub>2</sub> under low gate efficiency<sup>56,57</sup>. Further improvement could be achieved by integrating thinner high- $\kappa$  gate dielectrics or adopting local-gated architectures with shorter channel lengths.

In summary, our results suggest that the surface chemistry of sapphire critically influenced the domain orientation and quality of WS<sub>2</sub> films grown on the sapphire substrate via CVD. The observed changes upon air exposure may be explained by surface hydrolysis, potentially leading to the formation of aluminum (oxy)hydroxides and Al-rich surface reconstruction prior to growth, which in turn disrupts epitaxial alignment. Moreover, we found that UV irradiation prior to the CVD growth appears to effectively repair the surface by removing aluminum oxyhydroxide, restoring the sapphire to a state comparable to freshly annealed sapphire. The monolayer WS<sub>2</sub> film grown on repaired sapphire exhibits remarkable uniformity and mono-crystallinity. This UV light repair strategy should be effective for both small-scale and wafer-scale growth, offering a valuable method for producing high-performance 2D semiconductors for advanced electronic and optoelectronic applications.

## Methods

### Thermal annealing of sapphire substrates

Single-side polished c-plane sapphire substrates (001) were purchased from Princeton Scientific Corporation and Hefei Crystal Technical Materials. These substrates were fabricated to produce orientations of (0001) off **a** <1120> at 1.0° ± 0.1°, and off **m** <1010> directions at 0.5° ± 0.1°. As-received commercial sapphires typically exhibit low surface roughness (Ra <0.5 nm); however, they likely retain a significant density of residual defects and intrinsic surface stress as result of chemical mechanical polishing. For the engineering of atomic step heights of a sapphire, thermal annealing was conducted using a Carbolite RHF muffle furnace located within a cleanroom environment. The annealing process involved heating the substrates to 1250 °C at a rate of 5 °C/min and holding for 4 h to achieve an atomic step height of ~0.2 nm, and to 1350 °C for 4 h to achieve an atomic step height of ~1 nm.

### Aging sapphires in air

The freshly engineered sapphire substrates were exposed to an air environment within a cleanroom. Each substrate was placed on a petri dish lined with filter paper and subjected to various aging durations to assess the effects on surface chemistry and morphology.

### UV exposure in air

The aged sapphires were placed inside a Samco model UV-1 system. The substrates were exposed to UV light (wavelength of 320 nm to 400 nm, power density of 0.5 W/cm<sup>2</sup>) in an air for 30 min.

### Epitaxial growth of WS<sub>2</sub> monolayer

The epitaxial growth was carried out in a three-zone CVD system with a tube diameter of 70 mm. Sulfur powders (6.0 g, 99.998%, ALDRICH) were placed in the upstream of heating zone I and heated between 150–200 °C. WO<sub>3</sub> powders (99.995%, ALDRICH) and KCl (99.5%, ALDRICH) were positioned in heating zone II, and sapphire substrates were situated in heating zone III. The CVD process was conducted under low pressure within an argon atmosphere. Specifically, the growth temperatures of zone I, zone II and zone III were set at 180, 630, and 950 °C, respectively, with a gas flow of argon (400 sccm) and hydrogen (10 sccm). The pressure in the growth chamber was kept at 5 torr. The growth time varied, with 5–15 min for individual islands, and 30–40 min for a continuous film. Considering that the sulfur

concentration may vary from run to run and consequently influence domain orientation<sup>58</sup>, freshly annealed sapphire was systematically placed alongside the target sapphire for each growth run.

### Transfer of WS<sub>2</sub> monolayer using a polypropylene carbonate (PPC)-assisted method

Monolayer WS<sub>2</sub> films grown on sapphire were transferred onto SiO<sub>2</sub>/Si substrates using a wet transfer process assisted by polypropylene carbonate (PPC, Sigma-Aldrich). PPC was spin-coated onto the WS<sub>2</sub>/sapphire stack at 6000 r.p.m. for 1 min and subsequently baked at 90 °C on a hotplate for 1 min under ambient conditions. The sapphire substrate was then etched in a potassium hydroxide (KOH) solution at room temperature to release the PPC/WS<sub>2</sub> stack. The detached film was thoroughly rinsed with deionized water and transferred onto the target substrate. After transfer, the sample was gently dried under a nitrogen gas stream. PPC was removed by immersing the sample in anisole (Sigma-Aldrich) for 10 min, followed by sequential rinses in acetone, isopropyl alcohol (IPA), and ethanol. The sample was finally dried under nitrogen to ensure complete solvent removal.

**Device fabrication and electrical measurements.** Source and drain electrodes were defined using standard electron-beam lithography with 950 PMMA A4 as the electron-beam resist. Metal contacts comprising a 5 nm indium layer and a 50 nm gold capping layer were deposited by thermal evaporation at a base pressure of  $\sim 10^{-7}$  torr, with a deposition rate of 1 nm min<sup>-1</sup> for both layers. Lift-off was performed in acetone at room temperature for 30 min. All electrical transport measurements were carried out in a vacuum cryostat probe station under a base pressure of  $\sim 1 \times 10^{-4}$  mbar. Electrical characterization was performed using Keithley 2450 source meter units controlled via Python-based automation.

**Sample characterizations.** Raman and PL spectra were collected at room temperature using the confocal WiTec Alpha 300 R Raman Microscope (laser excitation, 532 nm). The surface profiles of sapphire samples were tested by Bruker's dimension icon AFM system. The XPS measurements for sapphire samples were conducted by a VG ESCALAB 220i-XL system with a monochromatic Al K $\alpha$  source and a pass energy of 10 eV, with electron flood gun filament current setting at 0–2.4 A. The XPS data of WS<sub>2</sub> were acquired with a hemispherical electron analyzer (SCIENTA HiPP-2) in normal emission condition, by using a monochromatized Al K $\alpha$  ( $h\nu = 1486.6$  eV) as energy excitation and energy resolution of  $\sim 0.3$  eV. The angle of photoemitted electron collection was set at 30° relative to the substrate normal. RHEED (STAIB Instruments) was measured at room temperature under an ultrahigh vacuum of  $10^{-9}$  torr. The electron acceleration voltage was 15 kV. Atomic-resolution STEM-ADF imaging was performed on an aberration-corrected JEOL ARM200F, equipped with a cold field-emission gun and an ASCOR corrector operating at 80 kV. The convergence semi-angle of the probe was around 30 mrad. Cross-sectional STEM lamellae of sapphire samples were prepared using a focused ion beam (FIB, FEI Helios Nanolab 600). For low-temperature circular dichroic photoluminescence (CDPL) measurements, the sample was kept in a cryostat on top of a motorized stage, and a 570 nm pulsed laser ( $\sim 80$  ps) was used for the excitation. The ARPES data were acquired in a custom-designed system, with a hemispherical electron analyzer (SCIENTA DA30L) and monochromatized HeI $\alpha$  ( $h\nu = 21.218$  eV) radiation source (SCIENTA VUV5k). Before ARPES measurement the WS<sub>2</sub> ML on HOPG was annealed at 200 °C x 12 h and 400 °C x 1 h to remove surface contaminants.

### Theoretical calculation

The adsorption energies of WS<sub>2</sub> monolayer on a c-plane Al<sub>2</sub>O<sub>3</sub> surface (without and with reconstructed surface) were calculated using density functional theory (DFT) with Perdew-Burke-Ernzerhof (PBE)

exchange-correlation functional as implemented in the Vienna ab initio simulation package (VASP)<sup>54–56</sup>. The cut-off energy for plane-wave basis set was set at 500 eV. The system was modeled as a triangular island of a monolayer WS<sub>2</sub> (4-unit cells on each side) on a 3-layer Al<sub>2</sub>O<sub>3</sub> substrate.  $6 \times 6$  supercell and  $(\sqrt{31} \times \sqrt{31})R90^\circ$  supercells were used for crystal and reconstructed Al<sub>2</sub>O<sub>3</sub> surfaces, respectively. The structures were optimized at  $\Gamma$  point until the Hellmann-Feynman forces on the atoms were less than 0.05 eV/Å. The DFT-D2 method of Grimme<sup>57</sup> was used to include the van der Waals interaction.

### Data availability

The Source Data underlying the figures of this study are available at <https://doi.org/10.6084/m9.figshare.29409821>. All raw data generated during the current study are available from the corresponding authors upon request.

### References

- Fiori, G. et al. Electronics based on two-dimensional materials. *Nat. Nanotechnol.* **9**, 768–779 (2014).
- Briggs, N. et al. A roadmap for electronic grade 2D materials. *2D Mater.* **6**, 022001 (2019).
- Lin, Y. et al. Realizing large-scale, electronic-grade two-dimensional semiconductors. *ACS Nano* **12**, 965–975 (2018).
- Akinwande, D. et al. Graphene and two-dimensional materials for silicon technology. *Nature* **573**, 507–518 (2019).
- Xu, Z. Q. et al. Synthesis and transfer of large-area monolayer WS<sub>2</sub> crystals: moving toward the recyclable use of sapphire substrates. *ACS Nano* **9**, 6178–6187 (2015).
- Choi, W. et al. Recent development of two-dimensional transition metal dichalcogenides and their applications. *Mater. Today* **20**, 116–130 (2017).
- Fu, J. et al. Oriented lateral growth of two-dimensional materials on c-plane sapphire. *Nat. Nanotechnol.* **18**, 1289–1294 (2023).
- Li, T. et al. Epitaxial growth of wafer-scale molybdenum disulfide semiconductor single crystals on sapphire. *Nat. Nanotechnol.* **16**, 1201–1207 (2021).
- Wang, J. et al. Dual-coupling-guided epitaxial growth of wafer-scale single-crystal WS<sub>2</sub> monolayer on vicinal a-plane sapphire. *Nat. Nanotechnol.* **17**, 33–38 (2022).
- Zhu, H. et al. Step engineering for nucleation and domain orientation control in WSe<sub>2</sub> epitaxy on c-plane sapphire. *Nat. Nanotechnol.* **18**, 1295–1302 (2023).
- Zheng, P. et al. Universal epitaxy of non-centrosymmetric two-dimensional single-crystal metal dichalcogenides. *Nat. Commun.* **14**, 592 (2023).
- Smink S., Majer L. N., Boschker H., Mannhart J., Braun W. Long-range atomic order on double-stepped Al<sub>2</sub>O<sub>3</sub> (0001) Surfaces. *Adv. Mater.*, **36**, 2312899 (2024).
- Mo, J. et al. Importance of the substrate's surface evolution during the MOVPE growth of 2D-transition metal dichalcogenides. *Nanotechnology* **31**, 125604 (2020).
- Barth, C. & Reichling, M. Imaging the atomic arrangements on the high-temperature reconstructed  $\alpha$ -Al<sub>2</sub>O<sub>3</sub> (0001) surface. *Nature* **414**, 54–57 (2001).
- Eng, P. J. et al. Structure of the hydrated  $\alpha$ -Al<sub>2</sub>O<sub>3</sub> (0001) surface. *Science* **288**, 1029–1033 (2000).
- Chambers, S. A., Droubay, T., Jennison, D. R. & Mattsson, T. R. Lamellar growth of ultrathin metal films on metal oxides: Co on hydroxylated  $\alpha$ -Al<sub>2</sub>O<sub>3</sub> (0001). *Science* **297**, 827–831 (2002).
- Aljarb, A. et al. Substrate lattice-guided seed formation controls the orientation of 2D transition-metal dichalcogenides. *ACS Nano* **11**, 9215–9222 (2017).
- Ranea, V. A., Carmichael, I. & Schneider, W. F. DFT investigation of intermediate steps in the hydrolysis of  $\alpha$ -Al<sub>2</sub>O<sub>3</sub> (0001). *J. Phys. Chem. C* **113**, 2149–2158 (2009).

19. Chen, X. et al. Atomistic mechanisms of water vapor-induced surface passivation. *Sci. Adv.* **9**, eadh5565 (2023).
20. Liu, Q., Tong, X. & Zhou, G. H<sub>2</sub>O dissociation-induced aluminum oxide growth on oxidized Al(111) surfaces. *Langmuir* **31**, 13117–13126 (2015).
21. Liu, Q., Qin, H., Boscoboinik, J. A. & Zhou, G. Comparative study of the oxidation of NiAl(100) by molecular oxygen and water vapor using ambient-pressure X-ray photoelectron spectroscopy. *Langmuir* **32**, 11414–11421 (2016).
22. Liu, P., Kendelewicz, T., Brown, G. E., Nelson, E. J. & Chambers, S. A. Reaction of water vapor with  $\alpha$ -Al<sub>2</sub>O<sub>3</sub>(0001) and  $\alpha$ -Fe<sub>2</sub>O<sub>3</sub>(0001) surfaces: synchrotron X-ray photoemission studies and thermodynamic calculations. *Surf. Sci.* **417**, 53–65 (1998).
23. Malki, A. et al. Calcination products of gibbsite studied by X-ray diffraction, XPS and solid-state NMR. *J. Solid State Chem.* **215**, 8–15 (2014).
24. Yue, Y. et al. Structure and reactivity of  $\alpha$ -Al<sub>2</sub>O<sub>3</sub> (0001) surfaces: How do Al-I and gibbsite-like terminations interconvert?. *J. Phys. Chem. C* **126**, 13467–13476 (2022).
25. Greczynski, G. & Hultman, L. Binding energy referencing in X-ray photoelectron spectroscopy. *Nat. Rev. Mater.* **10**, 62–78 (2025).
26. Moulder, J. F., Stickle, W. F., Sobol, P. E. & Bomben, K. D. *Handbook of X-ray photoelectron spectroscopy: a reference book of standard spectra for identification and interpretation of XPS data.* (ed. Chastain J.) (Perkin-Elmer Corporation, Physical Electronics Division, 1992).
27. Park, Y. et al. Critical role of surface termination of sapphire substrates in crystallographic epitaxial growth of MoS<sub>2</sub> using inorganic molecular precursors. *ACS Nano* **17**, 1196–1205 (2023).
28. Lee, W. & Park, S.-J. Porous anodic aluminum oxide: Anodization and templated synthesis of functional nanostructures. *Chem. Rev.* **114**, 7487–7556 (2014).
29. Zhou, J. et al. A library of atomically thin metal chalcogenides. *Nature* **556**, 355–359 (2018).
30. Yang, P. et al. Highly reproducible epitaxial growth of wafer-scale single-crystal monolayer MoS<sub>2</sub> on sapphire. *Small Methods* **7**, 2300165 (2023).
31. Cohen, A. et al. Tungsten oxide mediated quasi-van der Waals epitaxy of WS<sub>2</sub> on sapphire. *ACS Nano* **17**, 5399–5411 (2023).
32. Bagwell, R. B. & Messing, G. L. Effect of seeding and water vapor on the nucleation and growth of  $\alpha$ -Al<sub>2</sub>O<sub>3</sub> from  $\gamma$ -Al<sub>2</sub>O<sub>3</sub>. *J. Am. Ceram. Soc.* **82**, 825–832 (1999).
33. Eklund, P., Sridharan, M., Singh, G. & Bøttiger, J. Thermal stability and phase transformations of  $\gamma$ -amorphous-Al<sub>2</sub>O<sub>3</sub> thin films. *Plasma Process. Polym.* **6**, S907–S911 (2009).
34. Reichel, F., Jeurgens, L. P. H., Richter, G. & Mittemeijer, E. J. Amorphous versus crystalline state for ultrathin Al<sub>2</sub>O<sub>3</sub> overgrowths on Al substrates. *J. Appl. Phys.* **103**, 093515 (2008).
35. Wilson, S. J. The dehydration of boehmite,  $\gamma$ -AlOOH, to  $\gamma$ -Al<sub>2</sub>O<sub>3</sub>. *J. Solid State Chem.* **30**, 247–255 (1979).
36. Ramírez, L. P., Bournel, F., Gallet, J. J., Dudy, L. & Rochet, F. Testing the Cabrera–Mott oxidation model for aluminum under realistic conditions with near-ambient pressure photoemission. *J. Phys. Chem. C* **126**, 2517–2530 (2022).
37. Mortelmans, W. et al. Epitaxial registry and crystallinity of MoS<sub>2</sub> via molecular beam and metalorganic vapor phase van der Waals epitaxy. *Appl. Phys. Lett.* **117**, 033101 (2020).
38. Vig, J. R. UV/ozone cleaning of surfaces. *J. Vac. Sci. Technol. A* **3**, 1027–1034 (1985).
39. Sun, C., Zeng, R., Zhang, J., Qiu, Z. & Wu, D. Effects of UV-Ozone treatment on sensing behaviours of EGFETs with Al<sub>2</sub>O<sub>3</sub> sensing film. *Materials* **10**, 1432 (2017).
40. Yoon, K. H., Kim, H., Koo Lee, Y.-E., Shrestha, N. K. & Sung, M. M. UV-enhanced atomic layer deposition of Al<sub>2</sub>O<sub>3</sub> thin films at low temperature for gas-diffusion barriers. *RSC Adv.* **7**, 5601–5609 (2017).
41. Fons P., Iwata K., Niki S., Yamada A., Matsubara K.J.J.o.C.G. Growth of high-quality epitaxial ZnO films on  $\alpha$ -Al<sub>2</sub>O<sub>3</sub>. *J. Crystal Growth* **201**, 627–632 (1999).
42. Lauritsen, J. V. et al. Atomic-scale structure and stability of  $\sqrt{31}\times\sqrt{31}$  R  $\pm$  9° surface of Al<sub>2</sub>O<sub>3</sub> (0001). *Phys. Rev. Lett.* **103**, 076103 (2009).
43. Renaud, G., Villette, B. & Vilfan, I. Bourret A. Atomic structure of the  $\alpha$ -Al<sub>2</sub>O<sub>3</sub> (0001)  $\sqrt{31}\times\sqrt{31}$  R  $\pm$  9° reconstruction. *Phys. Rev. Lett.* **73**, 1825–1828 (1994).
44. Milakhin, D. S. et al. Peculiarities of the AlN crystalline phase formation in a result of the electron-stimulated reconstruction transition  $\sqrt{31}\times\sqrt{31}$  R  $\pm$  9° – (1  $\times$  1). *Appl. Surf. Sci.* **541**, 148548 (2021).
45. French, T. M. & Somorjai, G. A. Composition and surface structure of the (0001) face of  $\alpha$ -alumina by low-energy electron diffraction. *J. Phys. Chem.* **74**, 2489–2495 (1970).
46. Vermeersch, M., Sporken, R., Lambin, P. & Caudano, R. The AlAl<sub>2</sub>O<sub>3</sub> interface formation as studied by electron spectroscopies. *Surf. Sci.* **235**, 5–14 (1990).
47. Richmond, E. D. XPS analysis of the sapphire surface as a function of high temperature vacuum annealing. *MRS Online Proc. Lib.* **159**, 253–256 (1989).
48. Zhang, T., Wang, J., Wu, P., Lu, A.-Y. & Kong, J. Vapour-phase deposition of two-dimensional layered chalcogenides. *Nat. Rev. Mater.* **8**, 799–821 (2023).
49. Scrace, T. et al. Magnetoluminescence and valley polarized state of a two-dimensional electron gas in WS<sub>2</sub> monolayers. *Nat. Nanotechnol.* **10**, 603–607 (2015).
50. Plechinger, G. et al. Trion fine structure and coupled spin–valley dynamics in monolayer tungsten disulfide. *Nat. Commun.* **7**, 12715 (2016).
51. Bussolotti, F., Yang, J., Kawai, H., Chee, J. Y. & Goh, K. E. J. Influence of many-body effects on hole quasiparticle dynamics in a WS<sub>2</sub> monolayer. *Phys. Rev. B* **103**, 045412 (2021).
52. Bussolotti, F. et al. Electronic properties of atomically thin MoS<sub>2</sub> layers grown by physical vapour deposition: band structure and energy level alignment at layer/substrate interfaces. *RSC Adv.* **8**, 7744–7752 (2018).
53. Lim, Y. et al. Modification of vapor phase concentrations in MoS<sub>2</sub> growth using a NiO foam barrier. *ACS Nano* **12**, 1339–1349 (2018).
54. Llinas, J. P. et al. Short-channel field-effect transistors with 9-atom and 13-atom wide graphene nanoribbons. *Nat. Commun.* **8**, 633 (2017).
55. Lu, Z. et al. Wafer-scale high- $\kappa$  dielectrics for two-dimensional circuits via van der Waals integration. *Nat. Commun.* **14**, 2340 (2023).
56. Canto, B. et al. Multi-project wafer runs for electronic graphene devices in the European 2D-Experimental Pilot Line project. *Nat. Commun.* **16**, 1417 (2025).
57. Sebastian, A., Pendurthi, R., Choudhury, T. H., Redwing, J. M. & Das, S. Benchmarking monolayer MoS<sub>2</sub> and WS<sub>2</sub> field-effect transistors. *Nat. Commun.* **12**, 693 (2021).
58. Li, C. et al. Revisiting the epitaxial growth mechanism of 2D TMDC single crystals. *Adv. Mater.* **36**, 2404923 (2024).

## Acknowledgements

We acknowledge the funding support from the Agency for Science, Technology and Research Grant (C230917006). K.E.J.G. acknowledges a Singapore National Research Foundation Grant (CRP21-2018-0001) and the support from the National Research Foundation, Singapore through the National Quantum Office, hosted in A\*STAR, under its Centre for Quantum Technologies Funding Initiative (S24Q2d0009). The research is also supported by the Ministry of Education, Singapore, under its AcRF Tier 2 (MOE-T2EP50122-0016). C.S.L. acknowledges the support from A\*STAR under its MTC IRG grant no. M23M6c0103, MTC YIRG grant no. M21K3c0124, and NRF under the NRF CRP Frontier proposal no. F-CRP-2024-0091. The computational work was performed on

resources of the National Supercomputing Centre (NSCC), Singapore and the A\*STAR Computational Resource Centre (A\*CRC).

## Author contributions

W.F. and K.E.J.G. conceived the idea and designed the experiments. W.F. and T.M. fabricated all samples. UV treatment and analysis were contributed by H.M., W.F. and K.E.J.G. XPS measurements and analysis were performed by J.W.C., M.Z., F.B., K.E.J.G. and W.F. FIB sample preparation and STEM characterization were conducted by W.F., S.L.T., H.R.T., M.L. and M.B. AFM testing were carried out by W.F., Y.C. and A.S. Optical measurements were performed by D.H. ARPES experiments were performed by F.B. Material transfer, device fabrication and electrical measurements were contributed by W.F., R.L. and C.S.L. Theoretical calculations were carried out by H.K. RHEED analysis and discussion were contributed by M.B. and C.P.Y.W. All authors contributed to the preparation of the paper.

## Competing interests

The authors declare no competing interests.

## Additional information

**Supplementary information** The online version contains supplementary material available at <https://doi.org/10.1038/s41467-025-63452-9>.

**Correspondence** and requests for materials should be addressed to Wei Fu or Kuan Eng Johnson Goh.

**Peer review information** *Nature Communications* thanks Xiaozhi Xu and the other anonymous reviewer for their contribution to the peer review of this work. A peer review file is available.

**Reprints and permissions information** is available at <http://www.nature.com/reprints>

**Publisher's note** Springer Nature remains neutral with regard to jurisdictional claims in published maps and institutional affiliations.

**Open Access** This article is licensed under a Creative Commons Attribution-NonCommercial-NoDerivatives 4.0 International License, which permits any non-commercial use, sharing, distribution and reproduction in any medium or format, as long as you give appropriate credit to the original author(s) and the source, provide a link to the Creative Commons licence, and indicate if you modified the licensed material. You do not have permission under this licence to share adapted material derived from this article or parts of it. The images or other third party material in this article are included in the article's Creative Commons licence, unless indicated otherwise in a credit line to the material. If material is not included in the article's Creative Commons licence and your intended use is not permitted by statutory regulation or exceeds the permitted use, you will need to obtain permission directly from the copyright holder. To view a copy of this licence, visit <http://creativecommons.org/licenses/by-nc-nd/4.0/>.

© The Author(s) 2025

<sup>1</sup>Institute of Materials Research and Engineering (IMRE), Agency for Science Technology and Research (A\*STAR), 2 Fusionopolis Way, Innovis #08-03, Singapore 138634, Republic of Singapore. <sup>2</sup>Quantum Innovation Centre (Q.InC), Agency for Science Technology and Research (A\*STAR), 2 Fusionopolis Way, Innovis #08-03, Singapore 138634, Republic of Singapore. <sup>3</sup>Institute of High-Performance Computing (IHPC), Agency for Science, Technology and Research, 1 Fusionopolis Way, Connexis #16-16, Singapore 138632, Republic of Singapore. <sup>4</sup>Science, Mathematics and Technology, Singapore University of Technology and Design, 8 Somapah Road, Singapore 487372, Republic of Singapore. <sup>5</sup>Imec, Kapeldreef 75, Leuven 3001, Belgium. <sup>6</sup>Department of Materials Science and Engineering, National University of Singapore, 9 Engineering Drive 1, Singapore 117575, Republic of Singapore. <sup>7</sup>Centre for Quantum Technologies, National University of Singapore, 3 Science Drive 2, Singapore 117543, Republic of Singapore. <sup>8</sup>Department of Physics, National University of Singapore, 2 Science Drive 3, Singapore 117551, Republic of Singapore. <sup>9</sup>Division of Physics and Applied Physics, School of Physical and Mathematical Sciences, Nanyang Technological University, 50 Nanyang Avenue, Singapore 639798, Republic of Singapore. ✉ e-mail: [fu\\_wei@imre.a-star.edu.sg](mailto:fu_wei@imre.a-star.edu.sg); [kejgoh@yahoo.com](mailto:kejgoh@yahoo.com)